

Research Article

A Thermofluid Analysis of the Magnetic Nanoparticles Enhanced Heating Effects in Tissues Embedded with Large Blood Vessel during Magnetic Fluid Hyperthermia

Koustov Adhikary and Moley Banerjee

Department of Mechanical Engineering, Future Institute of Engineering and Management, Sonarpur Station Road, Kolkata 700150, India

Correspondence should be addressed to Moley Banerjee; moley_kb@yahoo.com

Received 14 October 2015; Revised 1 March 2016; Accepted 8 March 2016

Academic Editor: You Qiang

Copyright © 2016 K. Adhikary and M. Banerjee. This is an open access article distributed under the Creative Commons Attribution License, which permits unrestricted use, distribution, and reproduction in any medium, provided the original work is properly cited.

The thermal effect developed due to the heating of magnetic nanoparticles (MNPs) in presence of external magnetic field can be precisely controlled by the proper selection of magnetic absorption properties of the MNPs. The present paper deals with the numerical simulation of temperature field developed within or outside the tumor, in the presence of an external alternating magnetic field, using a thermofluidic model developed using ANSYS FLUENT®. A three-layer nonuniform tissue structure with one or two blood vessels surrounding the tumor is considered for the present simulation. The results obtained clearly suggest that the volumetric distribution pattern of MNPs within the tumor has a strong influence on the temperature field developed. The linear pattern of volumetric distribution has a strong effect over the two other types of distribution considered herein. Various other important factors like external magnetic field intensity, frequency, vascular congestion, types of MNP material, and so forth are considered to find the influence on the temperature within the tumor. Results show that proper selection of these parameters has a strong influence on the desired therapeutic temperature range and thus it is of utmost importance from the efficacy point of view of magnetic fluid hyperthermia (MFH).

1. Introduction

Neoplasm is a situation when the excessive growth of the cells takes place inside the living tissue, which results in the formation of tumor which may be solid or fluid filled. This growth of the cells can be either benign or malignant. Benign tumors cannot spread within the tissue and they are not generally harmful to the human health. Even though they do not seem to be cancerous, some may push the transiting artery which in turn may create severe pain or may damage the physiological condition [1]. On the other hand, malignant tumor cells can grow at a very fast rate, which results in invading the surrounding tissues or it may spread to other organs also [2]. This kind of tumor is known as cancer and may result in the death of the patient if untreated at proper time. The better known therapies like radiotherapy, chemotherapy, or hyperthermia play a very vital role in

healing the patient suffering from cancer. The hyperthermia used in addition to radiotherapy, chemotherapy, or any surgery procedure increases the survival rate of the patients [1].

The effectiveness of hyperthermia is very much dependent on the temperature achieved during the procedure along with the thermal dose [3]. A perfect hyperthermia process should be such that it should selectively destroy the tumor cells without damaging the surrounding cells inside the healthy tissue [4–7]. Though there are definite prescriptions for temperature (generally 43°C) and time (usually 60 minutes), it has been found that there may be variation of both temperature and time of delivery during the treatment procedure [8]. One of the serious limitations of hyperthermia is the heating of the tumor in a well-defined and well-localized manner which is difficult to be achieved, especially when the tumor is located deep inside the tissue [9].

Another important side effect of the hyperthermia procedure is overheating of the body surfaces.

In order to overcome the abovementioned limitations, numerous researchers have thought of the application of magnetic fluid in hyperthermia known as magnetic fluid hyperthermia (MFH), which is a minimally invasive procedure. In MFH procedure, nanofluid containing MNPs are injected in the presence of external magnetic field. This will prevent the unnecessary overheating of the surrounding tissues, since the MNPs will only absorb the magnetic field. Due to the potential application towards the cancer therapy for the last fifteen years or so, MFH draws considerable attention amongst different researchers [5, 10]. The heat generation due to the MNPs in the presence of external alternating magnetic field takes place because of Néel relaxation and Brownian rotation losses [11]. Several researchers [12–14] had already pointed out that the selection of MNP concentration is a very important factor for the temperature developed within the tumor without damaging the surrounding cells, which in turn certainly reduces the chances of the damaging side effects as observed in the other procedures [15].

In order to find out the velocity profile of the blood flow inside the artery a comprehensive study has been carried out by Horng et al. [16] using the pulsatile velocity profile. The result clearly shows that there is some minor change in the thermal lesion region of tissue which is observed for the variation of different flow velocity waveform.

In spite of the widespread application in the biomedical field, MFH has some limitations of its own when their exist one or more blood vessel transits of the tumor, since the presence of large blood vessel surrounding the tumor will greatly affect the thermal ablative area by acting as a heat sink [17].

Various researchers [16, 18–24] had already studied the effect of thermal condition developed within the tumor in the presence of large or small blood vessel using either numerical or theoretical way, but very few studies have been done till now, considering the variation of different important parameters like volumetric distribution, vascular congestion, and so forth. Since selection of these parameters is very important from the efficacy point of view of MFH, a rigorous study is essential for this.

In this paper, we investigate the temperature field induced by the heating of the MNPs within a primary tumor transited by the one or two significant blood vessels. Using a thermo-fluid model developed in ANSYS FLUENT, the thermal influence of blood flow in vessels on temperature field within the tumor is studied. The simulation allows the optimization of the main parameters involved in the heating process of the tumor.

2. Computational Domain and Mathematical Model

2.1. Physical Model. For the present study we consider two different types of tumor model as shown in Figure 1. In single artery transiting the tumor (SATT) model, we consider the existence of one single artery transiting the tumor, whereas

in countercurrent flow vessels transiting the tumor (CVTT) model, two different blood vessels of countercurrent flow direction have been considered. The computation domain is considered to be of cube shape and the dimension is taken as $0.08 \text{ m} \times 0.08 \text{ m} \times 0.08 \text{ m}$, in which x denotes the tissue depth from the skin surface. The tumor is assumed to be located at the center of the cubic-shaped computational domain, having dimension of 0.02 m . In most of the other studies, so far, the tumor is considered to be embedded inside the tissue, with uniform thickness of muscle and tissue, respectively, but here we consider the nonuniform thickness of three different layers along with the fact that the tumor is assumed to be embedded deep inside the body. The thickness ratio of skin, fat, and muscle is considered to be 1:4:15. Two different geometrical models of the tumor are considered in this paper. In CVTT model the center line of the two blood vessels is assumed to be shifted by 6 mm from the tumor center, whereas for the SATT model it has been assumed that the center line of the artery is passing through the tumor center.

2.2. Bioheat Transfer Model. In the paper, the well-known Pennes equation was adopted to model the heat transfer in biological tissues. It reads as

$$\rho_t c_t \frac{\partial T_t}{\partial t} = \nabla [\lambda_t \nabla T_t] - W_b c_b (T_t - T_b) + Q_{tm} + Q_r, \quad (1)$$

where ρ is the density, c is the heat capacity, λ is the thermal conductivity, W is the blood perfusion, Q_{tm} is metabolic heat generation, Q_r is the volumetric heat source due to spatial heat generation, and subscripts t and b denote tissue and blood, respectively.

For the large blood vessel domain, the temperature field can be described by

$$\rho_b c_b \left(\frac{\partial T_b}{\partial t} + \mathbf{V} \nabla T_b \right) = \nabla [\lambda_b \nabla T_b] + Q_r, \quad (2)$$

where \mathbf{V} is the blood velocity.

2.3. Boundary Condition. The large blood vessel is embedded in the center of tissues along x -direction. The blood is considered as a laminar flow. It is a reasonable assumption that the flow velocity of the blood is along x -direction and there is no flow across the y -direction, since the artery is parallel to the x -axis:

$$\text{Inlet BC: } V_x = 2V_0 \left(1 - \frac{r_b^2}{R_b^2} \right), \quad (3)$$

$$V_y = V_z = 0,$$

where V_0 is the center line velocity of the blood, r_b is the radial location, and R_b is the vessel radius.

The temperature $T_0 = 37^\circ\text{C}$ was considered on all the external surfaces of the geometry (Dirichlet boundary condition). At all the interfaces like skin-fat, tumor-artery, tumor-vain, and tumor-muscle, the Newman boundary conditions are imposed. The heat flux coming from the tumor is completely received by the blood vessel.

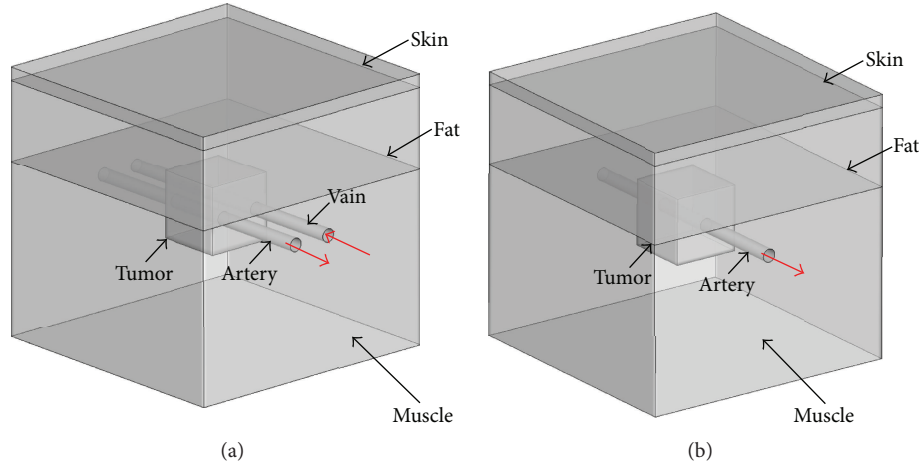


FIGURE 1: Schematic representation of the vascular model, showing the tumor, muscle fat, and skin separately: (a) countercurrent flow vessels, showing the existence of both artery and vein (CVTT), where the distance between the center line of the blood vessels is 12 mm, and (b) single artery transiting the tumor (SVTT) passing through the center of the tumor.

2.4. Mathematical Model for Heat Dissipation of MNPs in Presence of Magnetic Field. The magnetic particle will behave as a superparamagnetic particle in the presence of external magnetic field and this feature is the fundamental basis of MFH. The selection of the MNP and its quantity is very important in order to ensure the destruction of tumor cells due to the heating effect. This means that for optimal MFH treatment, a ferrofluid dose should be minimal and provide sufficient heat [25]. Taking into consideration the abovementioned facts a lot of effort has already been put to determine the optimal particle size [26] and type [27].

In the presence of an alternating magnetic field with high frequency, the MNPs loaded within tumor absorb heat due to the relaxation processes in the superparamagnetic regime. During this process the MNPs act as nanoheaters and the injection sites become the heating source of the tumor. For the uniform heating of the tumor tissue a suitable distribution of the injection sites is essential. Rosensweig [27] gives the expression of power dissipation of MNPs in an alternating magnetic field as

$$Q_r = \pi\mu_0\chi_0H_0^2f \frac{2\pi f\tau}{1 + (2\pi f\tau)^2}, \quad (4)$$

where $\mu_0 (= 4\pi \times 10^{-7} \text{ Tm/A})$ is the permeability of free space, χ_0 is the equilibrium susceptibility, H_0 and f are the amplitude and frequency of the alternating magnetic field, and τ is the effective relaxation time, given by

$$\frac{1}{\tau} = \frac{1}{\tau_N} + \frac{1}{\tau_B}, \quad (5)$$

where τ_N and τ_B are Néel relaxation and Brownian relaxation time, respectively. τ_N and τ_B are written as

$$\tau_N = \frac{\sqrt{\pi}}{2} \tau_0 \frac{\exp(\Gamma)}{\sqrt{\Gamma}}, \quad (6)$$

$$\tau_B = \frac{3\eta V_H}{kT},$$

where the shorter time constant tends to dominate in determining the effective relaxation time for any given size of particle. τ_0 is the average relaxation time in response to a thermal fluctuation, η is the viscosity of the medium, V_H is the hydrodynamic volume of the MNPs, k is the Boltzmann constant ($= 1.38 \times 10^{-23} \text{ J/K}$), and T is the temperature. Here, $\Gamma = KV_M/kT$, where K is the magnetocrystalline anisotropy constant and V_M is the volume of MNPs. The MNPs volume V_M and the hydrodynamic volume V_H are written as

$$V_M = \frac{4\pi r^3}{3}, \quad (7)$$

$$V_H = \frac{4\pi (r + \delta)^3}{3},$$

where r is the radius of MNP and δ is the thickness of adsorbed surfactant layer.

The equilibrium susceptibility χ_0 is assumed to be the chord susceptibility corresponding to the Langevin equation [$L(\zeta) = M/M_s = \text{Coth } \zeta - 1/\zeta$] and expressed as

$$\chi_0 = \chi_i \frac{3}{\zeta} \left(\text{Coth } \zeta - \frac{1}{\zeta} \right), \quad (8)$$

where $\zeta = \mu_0 M_d H V_M / kT$, $H = H_0 \text{Cos}(\omega t)$, $M_s = \phi M_d$, ϕ is the volume fraction of MNPs. Here, M_d and M_s are the domain and saturation magnetization, respectively. The initial susceptibility is given by

$$\chi_i = \frac{\mu_0 \phi M_d^2 V_M}{3kT}. \quad (9)$$

2.5. Parametric Investigation of Power Dissipation. Based on the abovementioned theory, we calculated the power dissipation for aqueous dispersion of monodispersed equiatomic fccFePt MNPs varying the diameter of MNP in adiabatic condition. For comparison, also the power dissipations for

TABLE 1: Physical properties of fccFePt and Magnetite MNPs.

Material	M_d (kA/m)	K (kJ/m ³)	c_p (J/kgK)	ρ (kg/m ³)
fccFePt	1140	206	327	15200
Magnetite	446	9	670	5180
Maghemite	414	4.7	746	4600

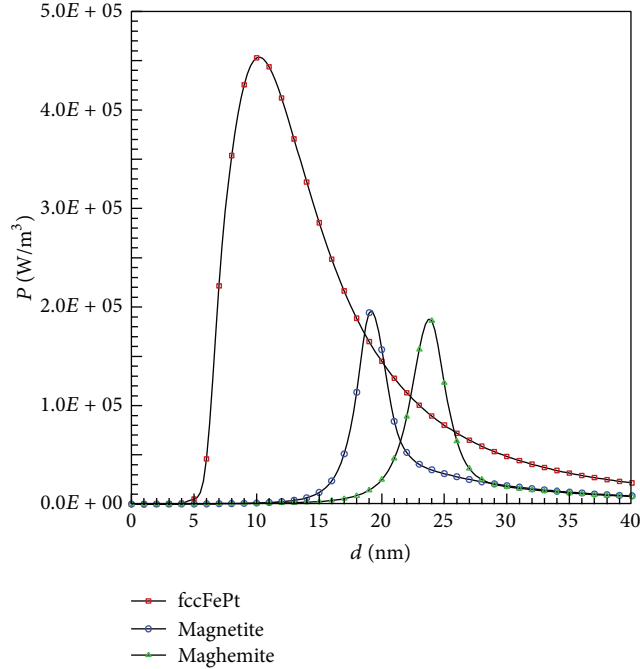


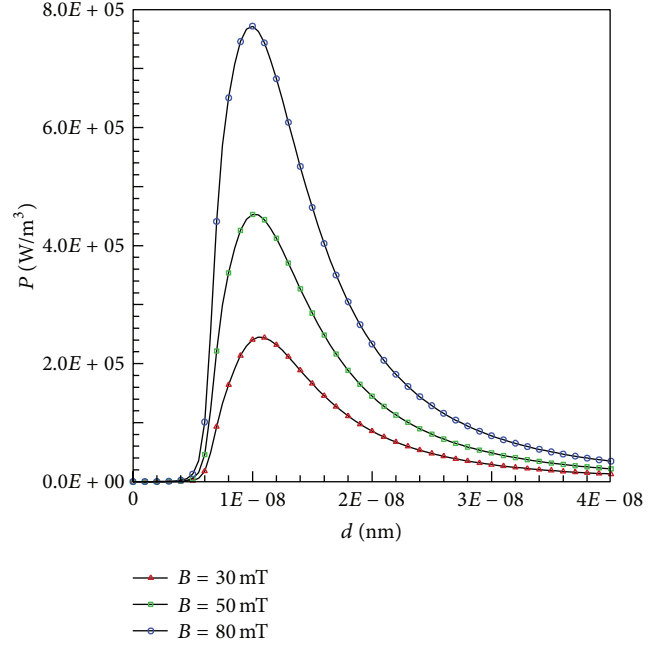
FIGURE 2: Variation of power dissipation with the particle size for various MNPs.

magnetite (Fe_3O_4) and maghemite ($\gamma\text{-Fe}_2\text{O}_3$) have been estimated.

In Table 1, physical properties of fccFePt, magnetite, and maghemite are shown [6].

Figure 2 shows comparative power dissipation for aqueous monodispersions of the various MNPs listed in Table 1, assuming $\tau_0 = 10^{-9}$ s and $\phi = 2 \times 10^{-5}$. Induction and frequency of applied magnetic field were fixed at $B_0 = \mu_0 H_0 = 50$ mT and 300 kHz. The carrier liquid is pure water in all cases. Surfactant layer thickness is assumed to be $\delta = 1$ nm. Figure 2 shows the gradual increase in power as the MNP size increases and it reaches a maximum value, beyond which it again drops. On these conditions, fccFePt MNPs yield the largest power dissipation. The size of the MNP (d_{\max}) at which this power is maximum is found to be 10.5, 19 and 23 nm for three different magnetic materials considered herein.

Figure 3 shows the dependence of power dissipation on induction of applied magnetic field, for fixed value of frequency ($= 300$ kHz), volume fraction ($\phi = 2 \times 10^{-5}$), and surfactant layer thickness ($\delta = 1$ nm). Three different values of B_0 are considered, namely, 30, 50, and 80 mT. The result shows that there is a gradual increase as the induction value

FIGURE 3: Variation of power dissipation with the particle size for various B_0 .

increases. It is also interesting to note that there is no change in d_{\max} value.

Figure 4 shows the dependence of power dissipation on the frequency of applied magnetic field, keeping the other parameters same as the previous one. Three different values of f are considered, namely, 100, 200, and 300 kHz. The result shows that there is a gradual increase in the heating value with the increase in the frequency. It is also observed from the result that as the frequency value decreases, d_{\max} also increases. It is 13.5 for 200 kHz while it becomes 16.2 nm for 100 kHz.

Figures 5 and 6 show the variation of power dissipation with volume fraction and surfactant layer thickness, respectively. From the result it is quite clear that as the volume fraction increases the power dissipation increases, while there is no change in the d_{\max} value.

On the other hand the increase in surfactant layer thickness gradually decreases the power dissipation value, while d_{\max} value reduces.

Specific absorption rate (SAR) is a measure of the rate at which energy is absorbed by the human body when exposed to a radio frequency (RF) electromagnetic field, although it can also refer to absorption of other forms of energy by tissue, including ultrasound. It is defined as the power absorbed per mass of tissue. Assuming a constant value for the magnetic susceptibility, the SAR within the tumor tissue can be calculated from

$$\text{SAR} = \frac{P}{\rho_{\text{MNP}}\phi}, \quad (10)$$

where ρ_{MNP} is the nanoparticle density. Figure 7 represents the variation of SAR with particle size for three different magnetic materials considered herein. From the result it is

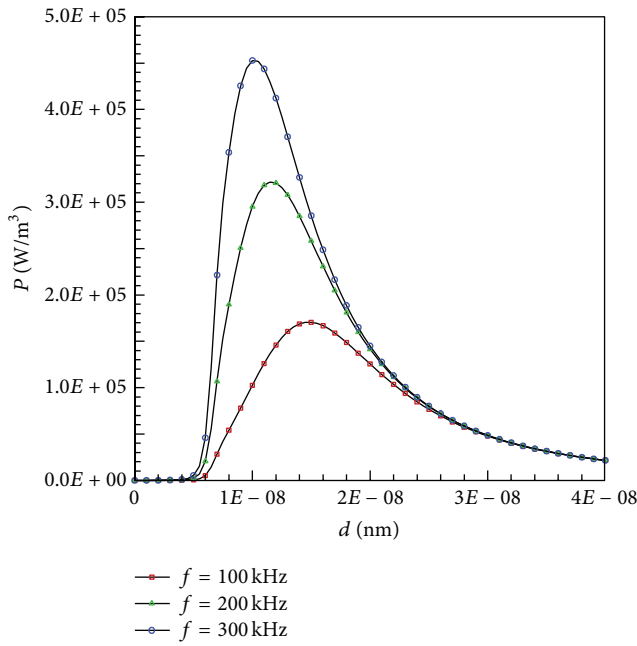


FIGURE 4: Variation of power dissipation with the particle size for various f .

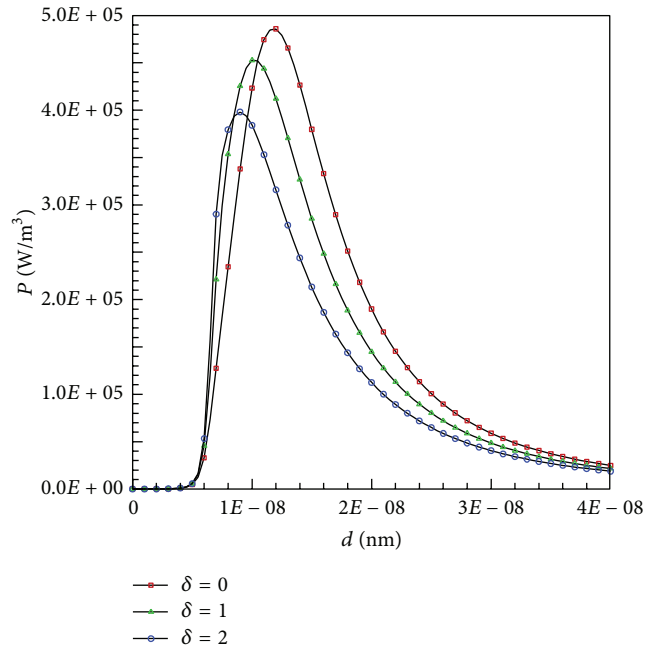


FIGURE 6: Variation of power dissipation with the particle size for various δ .

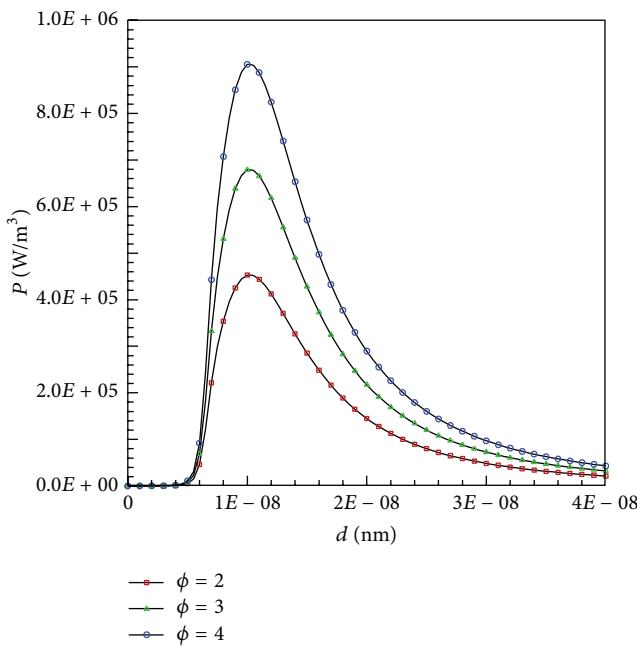


FIGURE 5: Variation of power dissipation with the particle size for various ϕ .

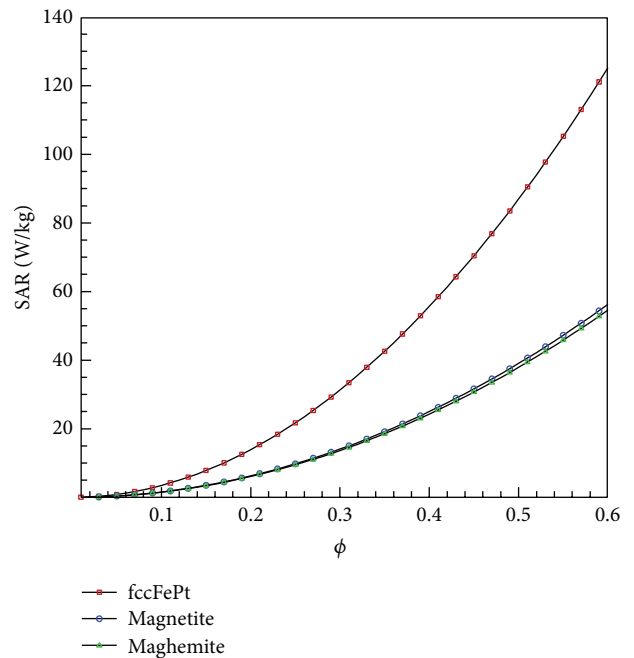


FIGURE 7: Variation of SAR with particle concentration for various magnetic materials.

quite clear that the fccFePt material shows the highest value of SAR at a particular particle size compared to its two other counterparts. Hence in order to study the further variation, we select the fccFePt material for the consideration.

Figure 8 shows the variation of SAR with different particle size. Four different particle sizes have been considered, namely, 10, 15, 20, and 30 nm, respectively. The result clearly

indicates that as the particle concentration increases gradually the SAR value increases but this increment takes place at a very faster rate for higher particle size compared to the case when the particle size is less.

From these results it is quite clear that concentration of MNP, external magnetic field strength, and frequency all are quite important parameters for the temperature

TABLE 2: Thermophysical properties of different component.

Property	Skin	Fat	Muscle	Tumor	Blood	MNP
Thermal Conductivity (k [W/mK])	0.3	0.21	0.59	0.59	0.59	40
Blood perfusion rate (W_b [kg/s·m ³])	0.4	0.25	0.5	2	—	—
Mass density (ρ [kg/m ³])	1000	850	1050	1050	1050	5180
Heat capacity (c [J/kgK])	3770	2300	3750	3750	3750	4000
Metabolic heat production rate (Q_m [W/m ³])	368.1	368.3	684.2	684.2	—	—
Thickness (d [mm])	4	24	52	20	—	—

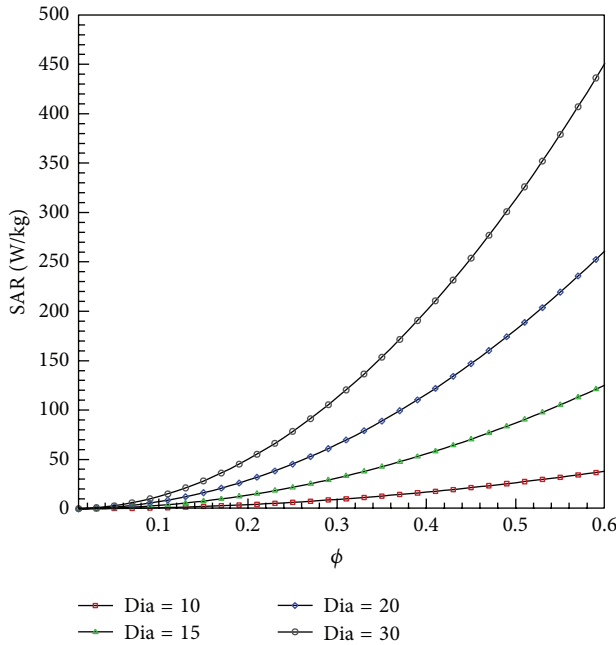


FIGURE 8: Variation of SAR with particle concentration for various particle size.

distribution inside the tumor and its surrounding healthy tissue.

Iron oxides magnetite Fe_3O_4 nanoparticles are the most studied to date due to their biocompatibility, when injected in the human tissue [5]. The superparamagnetic particles (10–40 nm) are recommended in clinical application as they are able to generate substantial heat within low magnetic field strength and frequency. The selection of frequency and field amplitude is very important parameter from the safe exposure and tolerance for the ablation of the tumor point of view. The selection of both frequency and magnetic field amplitude is governed by the Herget condition [12]: $H \times f < 5 \times 10^9$.

The typical magnetite dosage is ~ 10 mg MNPs per gram of tumor that has been reported in clinical studies [9]. Therefore the homogenous volume fraction is $\phi_h = 2.046 \times 10^{-3}$. Here we consider three cases for the distribution of a constant amount of MNPs inside the tumor. For each case the volume

fraction (ϕ) as a function of distance from the center of the tumor can be modeled as follows:

Homogenous distribution: $\phi = \phi_h$,

Linear distribution: $\phi = 4\phi_h \left(1 - \frac{r}{R}\right)$, (11)

Parabolic distribution: $\phi = 2.5\phi_h \left(1 - \frac{r^2}{R^2}\right)$.

One should note that (4) is valid for magnetic nanoparticles with strong reduced anisotropy [28] ($\sigma_a \gg 1$), where $\sigma_a = KV_M/kT$.

Taking the values from Table 1, one can calculate that $\sigma_a \approx 25.4$, which fulfills the condition for strong reduced anisotropy.

2.6. Model Parameters. For the abovementioned three-layer tissue structure, the thermal and physiological properties for each layer are very different. The magnitudes for all the parameters are listed in Table 2.

The temperature rise and its distribution in the human tissues are determined by a number of factors such as the thermophysical properties of the tissue like heat capacity and thermal conductivity, geometry, heat production due to metabolic processes, heat flow due to perfusion of blood, and finally heat generated by tissues due to electromagnetic excitation. Thus, if an additional substance is injected into the tissue, these parameters change and the model of the mixture has to be developed [29]:

$$\rho_{\text{mix}} = \phi \rho_{\text{MNP}} + (1 - \phi) \rho_{\text{tumor}}, \quad (12a)$$

$$c_{\text{mix}} = \phi c_{\text{MNP}} + (1 - \phi) c_{\text{tumor}}, \quad (12b)$$

$$\frac{1}{k_{\text{mix}}} = \frac{\phi}{k_{\text{MNP}}} + \frac{(1 - \phi)}{k_{\text{tumor}}}, \quad (12c)$$

where ρ , c , and k stand for density, specific heat, and thermal conductivity, respectively.

3. Results and Discussion

3.1. Numerical Solution Methods. ANSYS FLUENT [30] is used to solve the coupled fluid flow and the heat transfer with the velocity tolerance of 10^{-5} and the temperature

residue as 10^{-7} , by solving the unsteady Navier-Stokes and the energy equation simultaneously. Central differencing scheme of second-order accuracy is used to discretize the diffusion terms, whereas the convective terms are discretized by using power law scheme. The coupling of pressure velocity is done with Semi-Implicit Method for Pressure-Linked Equations (SIMPLE) technique, where the underrelaxation parameter for pressure and energy is taken to be 0.3 and 1.0, respectively.

A user defined function (UDF) is written and then compiled into FLUENT to incorporate the heating effect due to the injection of MNPs.

A fixed time stepping method is used with a step size of 0.1 sec and for a total exposure time of 1200 sec.

3.2. Grid Independence. The physical domain was discretized into a large number of quadrilateral computational cells. Model was tested for three different grid densities, that is, 1,50,000, 2,86,000, and 3,50,000 cells in the domain. The absolute difference in the maximum temperature at the center of the origin between the coarse and fine cross-sectional mesh was 3.5°C and that between fine and finer one was only 0.05°C , which was very small compared to the maximum temperature of around 45°C for the given input condition. Therefore, we adopted the scheme that contained number of elements 2,86,000 for the whole mesh as shown in Figure 2 that gave the best grid independency and stability in solution within a reasonable CPU time. Computations were carried out on a Microsoft Windows⁷ Ultimate workstation with Intel[®] Core[™] i7-3770, 3.40 GHz processor with 16 GB random access memory (RAM), and 2 TB hard drive available at the DST sponsored project laboratory. The average CPU time for one set of calculations was 125 min.

3.3. Code Validation. Two concentric spherical regions were chosen as the domain of the analysis in order to validate the results with the work of Lin and Liu [7]. The inner ($R_1 = 50$ mm) and outer sphere ($R_2 = 150$ mm) represent the tumor and the healthy tissue region, respectively. Transient form of Pennes BHE (see (1) and (2)) is solved for the two different magnetic materials, namely, 9 nm fccFePt and 19 nm magnetite, with the following thermophysical properties (subscripts 1 and 2 are for tumor and healthy tissue, resp.).

$k_1 = k_2 = 0.502$ W/mK, $W_{b1} = W_{b2} = 0.0064$ s⁻¹, $Q_{m1} = Q_{m2} = 540$ W/m³, $\rho_{\text{MNP}} = 15200$ kg/m³ for fccFePt and 5180 kg/m³ for magnetite, respectively, $c_{p\text{MNP}} = 327$ J/kgK for fccFePt and 670 J/kgK for magnetite, respectively, $\rho_2 = 1060$ kg/m³, $c_{p2} = 3600$ J/kgK, $\rho_b = 1000$ kg/m³, $c_{pb} = 4180$ J/kgK, $T_b = 37^\circ\text{C}$, and $\phi = 2 \times 10^{-5}$. The density, specific heat, and conductivity of the tumor will change due to the injection of the MNP and the corresponding values are calculated based on ((12a)–(12c)).

From the foregoing analysis of described in Section 2.5, we can calculate that in a magnetic field with fixed amplitude and frequency at 50 mT and 300 kHz and a volume fraction of $\phi = 2 \times 10^{-5}$, 9 nm fccFePt and 19 nm magnetite MNPs dissipate 3.97×10^5 W/m³ and 1.95×10^5 W/m³, respectively. These two values of power dissipation are used

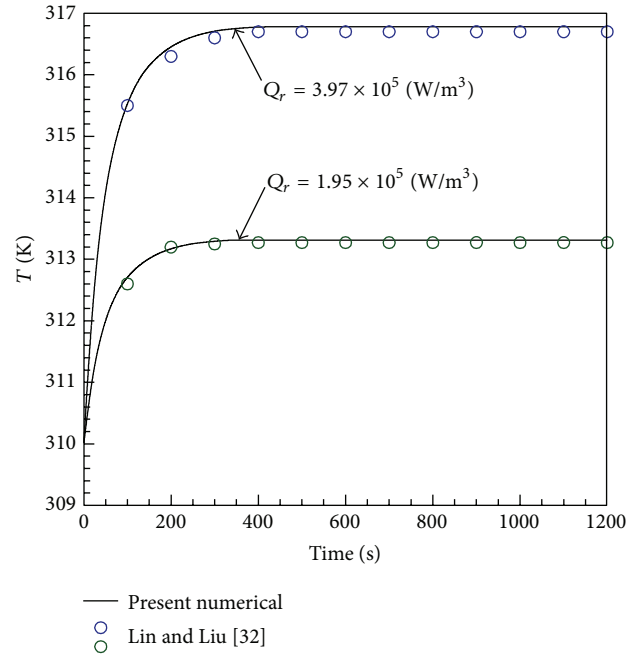


FIGURE 9: Comparison of the temperature history with time for the two different magnetic materials at the center of the tumor.

in the calculation, so that the result can directly be compared with Lin and Liu [7].

Figure 9 shows the history of temperature at the center of the tumor for the cases of 9 nm fccFePt and 19 nm magnetite MNPs. The result is plotted for 1200 sec, though it is quite clear from the result that the values become almost steady after 600 sec, which is certainly in accordance with the findings of Lin and Liu [7]. Also, Figure 10(a) shows the radial distribution of temperature in the tissue at 600 sec for the cases of 9 nm fccFePt and 19 nm magnetite MNPs. It is observed that the results of the present work match well with those given in the literature. In order to validate the same numerical model with the experimental studies, further results have been compared taking into consideration the experimental data. Figure 10(b) represents the variation of radial temperature distribution, when compared with the present simulation result and the experimental data from Miaskowski and Sawicki [31], where the temperature field is measured inside a tumor located inside a simplified female breast phantom. The comparison shows quite a good agreement with our numerical result. This ensures the validation of the present numerical model.

3.4. Comparison of Induced Temperature Increase for Tissue with or without Blood Vessel. The temperature field in the tumor computed as a solution of (1) and (2) depends on various parameters like size and thermal and magnetic properties of the MNP and thermal properties of healthy and diseased tissue along with the presence of large blood vessel. Transient form of (1) and (2) is solved for 1200 sec for all the results considered herein, in order to get the steady state response of temperature variation.

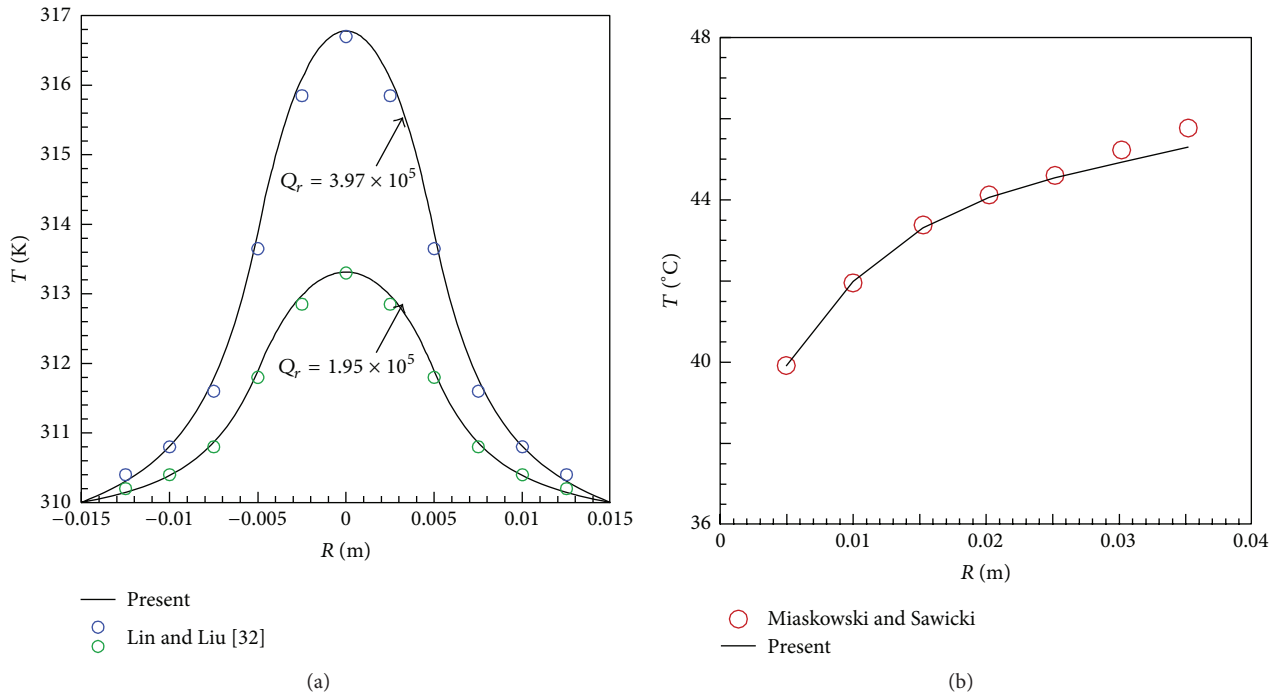


FIGURE 10: (a) Comparison of the temperature distribution inside the tissue at 600 sec for the two different magnetic materials. (b) Comparison of radial variation of temperature between experimental data and the present simulation.

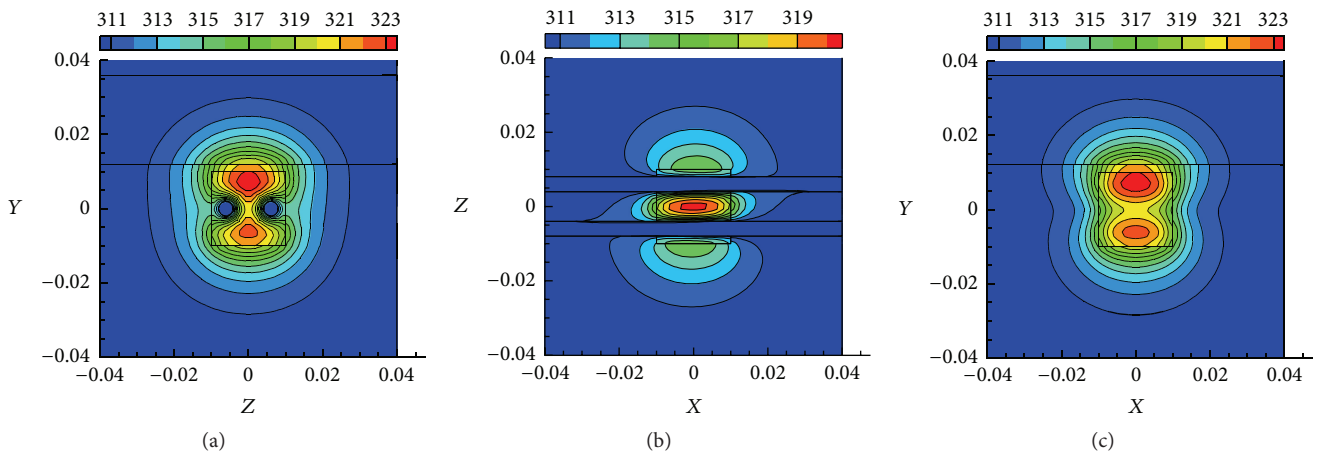


FIGURE 11: Spatial temperature distribution at time $t = 20$ min, using 9 nm fccFePt MNP: (a) x -plane, (b) y -plane, and (c) z -plane, taking center of the tumor as origin.

For all the simulation the magnetic field with fixed amplitude and frequency of 50 mT and 300 kHz with a volume fraction of $\phi = 2 \times 10^{-5}$ is considered, which produces a volumetric heat generation of $3.97 \times 10^5 \text{ W/m}^3$ for 9 nm fccFePt MNP.

3.4.1. Results for CVTT Model. Figure 11 shows the temperature fields inside the domain, when the tumor is transited by two blood vessels. The results are plotted along different plane

which certainly provides the clear evidence of cooling effect due to the presence of blood vessel.

Figure 11(a) clearly shows the existence of two blood vessels which act as a sink for the hyperthermia process. Due to the cooling effect induced by the blood vessels within the tissue, the temperature values decrease suddenly in their vicinity. The temperature on the tumor boundary is very close to the therapeutic temperature. The presence of blood vessel also prevents the damage of healthy tissue due to the overheating by providing the cooling effect. The maximum

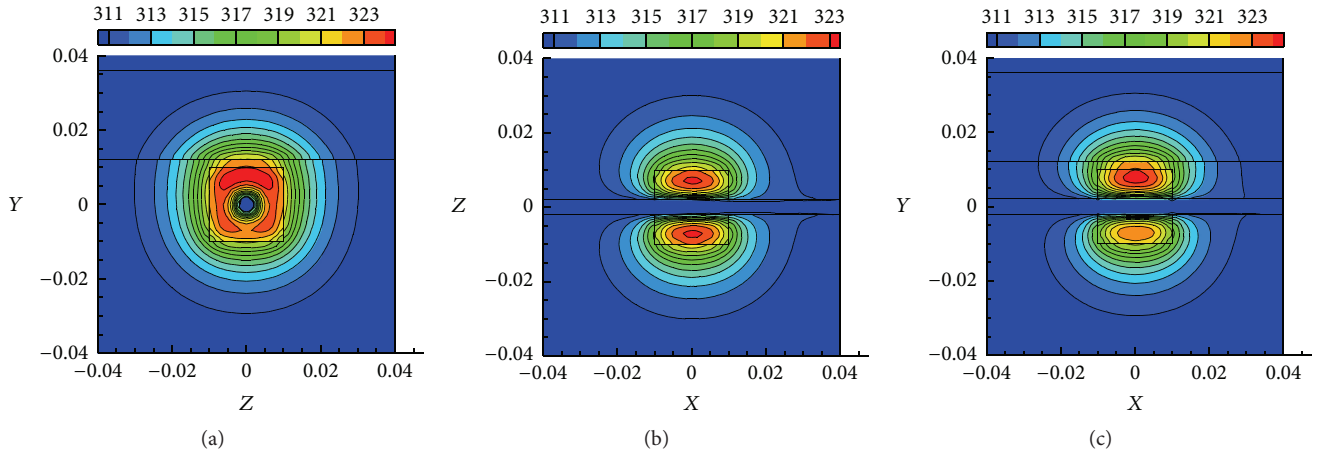


FIGURE 12: Spatial temperature distribution at time $t = 20$ min, using 9 nm fccFePt MNP: (a) x -plane, (b) y -plane, and (c) z -plane, taking center of the tumor as origin.

temperature observed with the abovementioned parameters is found to be around 323 K.

3.4.2. Results for SATT Model. Figures 12(a), 12(b), and 12(c) represent the temperature profile across three different planes for the SATT model. From the temperature contour it is quite evident that now the cooling effect is much less compared to the CVTT model. The temperature variation inside the tumor also shows a slight higher value compared to its counterpart.

3.4.3. Results for No Vessel Model. The cooling effect produced due to the presence of large blood vessel transiting the tumor certainly decreases the temperature near the vicinity of the blood vessel from the prescribed therapeutic temperature limits. If there is no blood vessel present inside the tumor, then the entire tumor is subjected to more or less uniform type of heating as represented in Figure 13. From the temperature profile it is quite clear that a maximum temperature of 332 K is observed for the present case, which is almost 9 K higher than the other two models considered earlier.

3.4.4. Axial Variation of Temperature. In order to get more insight into the problem, next we focus our attention on the axial variation of temperature. We define the line joining $(-0.04, 0, 0)$ and $(0.04, 0, 0)$ as the x -axis and the line joining $(0, 0, -0.04)$ and $(0, 0, 0.04)$ as the z -axis to plot all the axial variation of temperature for the CATT and the tumor modeled with and without any blood vessel. Since the central axis is parallel to the flow axis for the SATT model, we prefer to define the line joining $(-0.04, 0.005, 0)$ and $(0.04, 0.005, 0)$ as the x -axis while keeping the same definition for the z -axis.

Figures 14(a) and 14(b) give the axial variation of temperature for the three different geometrical models of tumor considered herein. Figure 14(a) indicates the gradual increase in temperature because of the presence of MNP and it has been observed that a maximum temperature is observed at the center of the tumor ($x = 0$), for all the three models. A

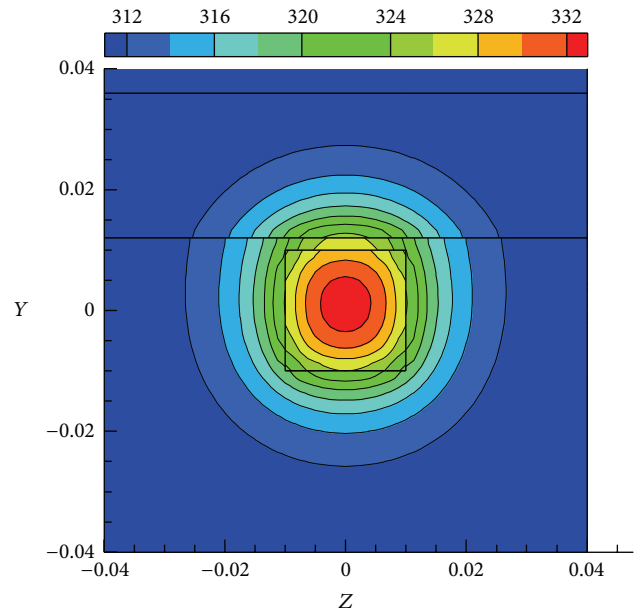


FIGURE 13: Spatial temperature distribution at time $t = 20$ min, using 9 nm fccFePt MNP, along x -plane, taking center of the tumor as origin.

closer look also reveals that there is considerable variation in temperature profile within $-0.02 \leq x \leq +0.02$ and outside the tumor region ($x \geq -0.02$ or $x \geq +0.02$) also. Since the cooling effect is less for the SATT model compared to the CVTT model, the maximum temperature is almost 323 K for the SATT model, whereas it is almost 320 K for the CATT model. On the other hand the maximum temperature is almost 333 K for the case when there is no vessel.

Results of Figure 14(b) show that the temperature profile drops to almost surrounding tissue temperature at the region when it comes closer to the large blood vessel. This drop will occur twice for the CVTT model, whereas it occurs once for the SVTT model. Hence, it can be concluded that the

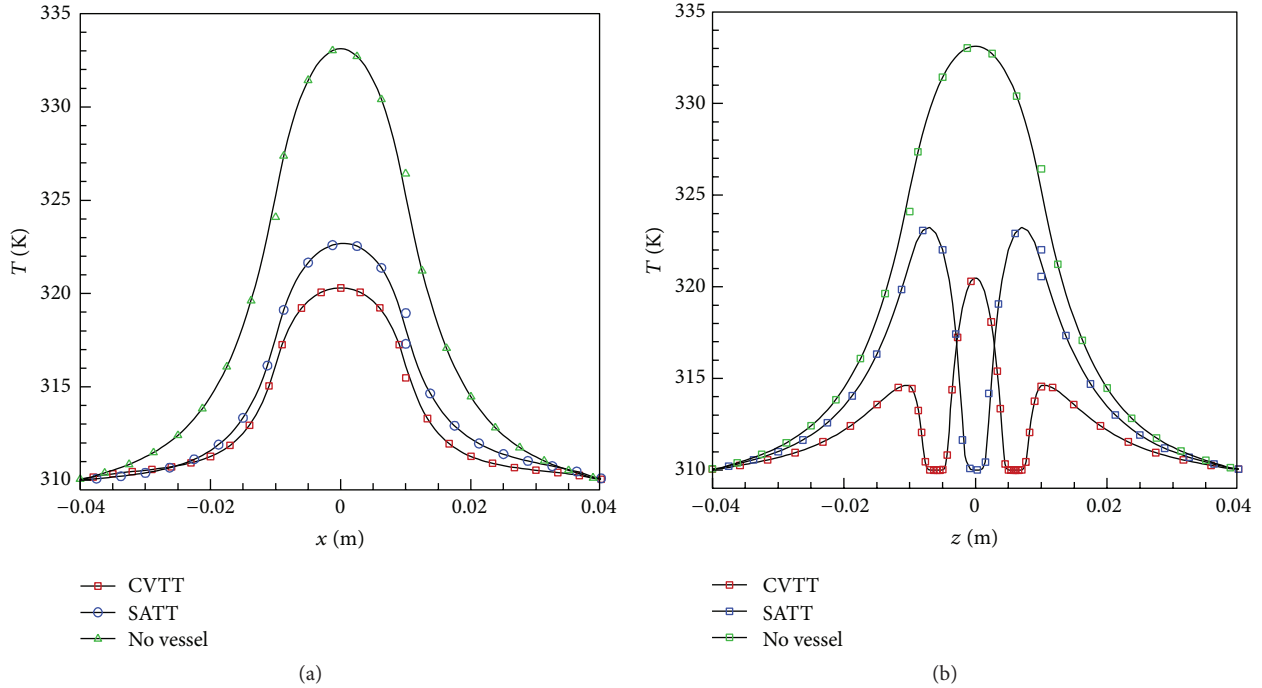


FIGURE 14: Axial variation of temperature profile for different vascular model using 9 nm fccFePt ($Q_r = 3.97 \times 10^5 \text{ W/m}^3$) as the MNP material: (a) along x -direction and (b) along z -direction.

presence of blood vessel produces a local minimum value of temperature, which certainly reduces the temperature in a large space inside the tumor, around the blood vessel, where the possibility that locally the temperature is below that of the therapeutic range appears. From the result of Figure 14(b) it is also clear that the zone where this lower temperature prevails is much longer for the CVTT model compared to the SATT model.

3.5. Comparison of Induced Temperature Increase for Different Magnetic Materials Considering CVTT Model. Once we find the effect of different geometrical model of tumor on the induced temperature using fccFePt as the magnetic material, we find that the CVTT model is more critical to attain the therapeutic temperature. Hence, in this phase we concentrate our attention on the variation of induced temperature for the CVTT model only, considering three different types of magnetic material (see Table 1).

For the simulation purpose we use 10.5 nm fccFePt, 19 nm magnetite, and 23 nm maghemite as the magnetic material, keeping the same value of amplitude and frequency as 50 mT and 300 kHz with a volume fraction of $\phi = 2 \times 10^{-5}$. The volumetric heat generation due to the external source for the above input parameters for the three materials will be 4.65×10^5 , 1.95×10^5 , and $1.87 \times 10^5 \text{ W/m}^3$, respectively.

Results of Figures 15(a) and 15(b) clearly indicate that the prediction of temperature is almost same for maghemite (315.1 K) and magnetite (314.9 K) material, whereas fccFePt predicts quite a high value of temperature (almost 322 K). Iron oxide magnetite Fe_3O_4 nanoparticles are biocompatible when injected in the human tissue and are most studied

till date. Hence the superparamagnetic particles (10–40 nm) are recommended in clinical application as they are able to generate substantial heat within low magnetic field strength and frequency.

Hence, we consider the magnetite as the material for all the simulation that we considered from this point onwards.

3.6. Parametric Investigation for Both SATT and CVTT Model.

Once the material for the MNP is selected the next task is to study the parametric investigation, in order to get the better insight of the problem and to find out the various factors on which the efficacy of the MFH depends.

3.6.1. Variation with External Magnetic Field Amplitude.

Three different values of field amplitude are considered as $H_0 = 5, 10,$ and 15 kA/m , while the external frequency and concentration are kept constant at 100 kHz and 2×10^{-5} , respectively. The corresponding value of Q_r can be calculated as $2.64 \times 10^5, 7.08 \times 10^5,$ and 1.16×10^6 , respectively. Comparing the results of Figures 16(a) and 16(c), we can find that both CVTT and SATT models predict that the temperature within and outside the tumor will gradually increase as the external field strength increases. For a smaller value of field strength like 5 kA/m the difference in maximum temperature prediction between CVTT model (316 K) and SATT model (317.5 K) is almost 1.5 K, whereas when the field strength increases to 15 kA/m this difference becomes almost 7.6 K.

Comparing the axial variation of temperature for the z -direction (Figures 16(b) and 16(d)), it is quite clear that the

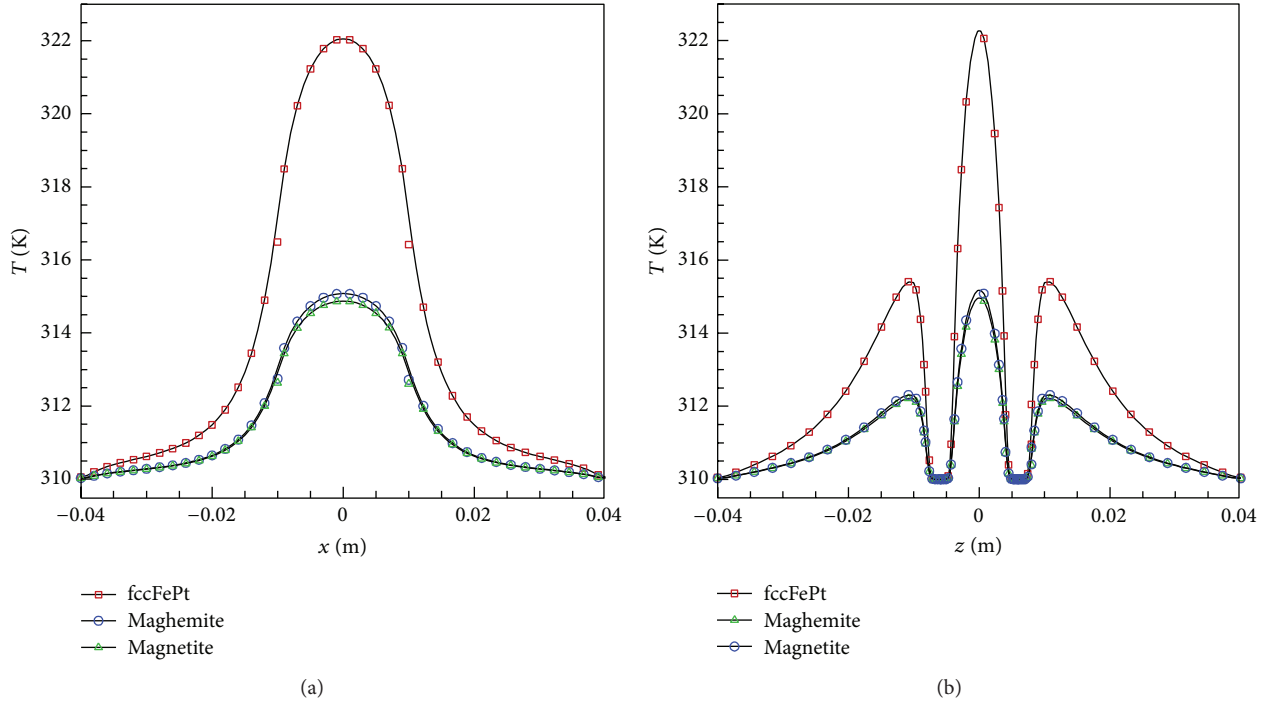


FIGURE 15: Axial variation of temperature profile for different magnetic material: (a) along x -direction and (b) along z -direction.

lower temperature zone prevails for much longer portion for the CVTT model compared to its counterpart.

3.6.2. Variation with Frequency. Three different values of frequency are considered as $f = 50, 100,$ and 150 kHz, while the external magnetic field strength and concentration are kept constant at 10 kA/m and 2×10^{-5} , respectively. The corresponding value of Q_r can be calculated as 1.87×10^5 , 7.08×10^5 , and 1.47×10^6 , respectively. Figures 17(a) and 17(b) show the axial variation of temperature for the CVTT model, while Figures 17(c) and 17(d) represent the same for the SATT model. Results show that as the frequency value increases the temperature increases both within the tumor and outside the tumor region. The increase in frequency value from 50 kHz to 150 kHz results in almost an increase of 33.75 K in maximum value of temperature for the CVTT model, this is, almost 42.45 K for the SATT model.

3.6.3. Variation with Inlet Velocity due to Vascular Congestion. Vascular congestion would greatly decrease the blood flow velocity. In all the above calculations discussed so far, the center line velocity is taken to be as 0.1 m/s. To assess the effect of vascular congestion caused by the MNPs on temperature distribution, it is assumed that the flow velocity of blood drops to 0.01 m/s.

Figures 18(a) and 18(b) show the axial variation of temperature for the CVTT model, while Figures 18(c) and 18(d) represent the same for the SATT model. The results clearly indicate that lowering the flow velocity of blood can significantly enhance the heating effect (≈ 5 K for the CVTT

model and ≈ 4.25 K for the SATT model), thereby reducing the cooling effect.

3.6.4. Variation with Concentration. Three different values of MNPs concentration are considered as $\phi = 5, 10,$ and 15 mg/gm, of tumor, while the external field and frequency are kept constant at 10 kA/m and 100 kHz, respectively. The corresponding value of Q_r can be calculated as 3.54×10^5 , 7.08×10^5 , and 1.06×10^6 , respectively. In this case also the results show the gradual increase of temperature along the axial direction with the increase in drug concentration. It is also observed from the diagram that the temperature reaches local maxima at the center of the tumor, which is certainly in line with the earlier observations made. This is true for both CVTT and SATT model (ref. Figures 19(a) and 19(c)). The corresponding axial variation along z -direction (Figures 16(b) and 16(d)) shows the existence of lower temperature zone close to the blood vessel. Since the effect of cooling is somewhat less for the SATT model, the maximum temperature measured at the tumor center is always higher compared to the values predicted by the CVTT model (ref. Figures 19(b) and 19(d)).

3.6.5. Variation with Concentration Distribution. The proper selection of MNPs concentration is one of the important parameters from the efficacy point of view of MFH. As discussed earlier here, two different types of drug distribution pattern are assumed within the tumor instead of assuming that the entire tumor is dosed with a homogenous concentration of drug as defined by (11).

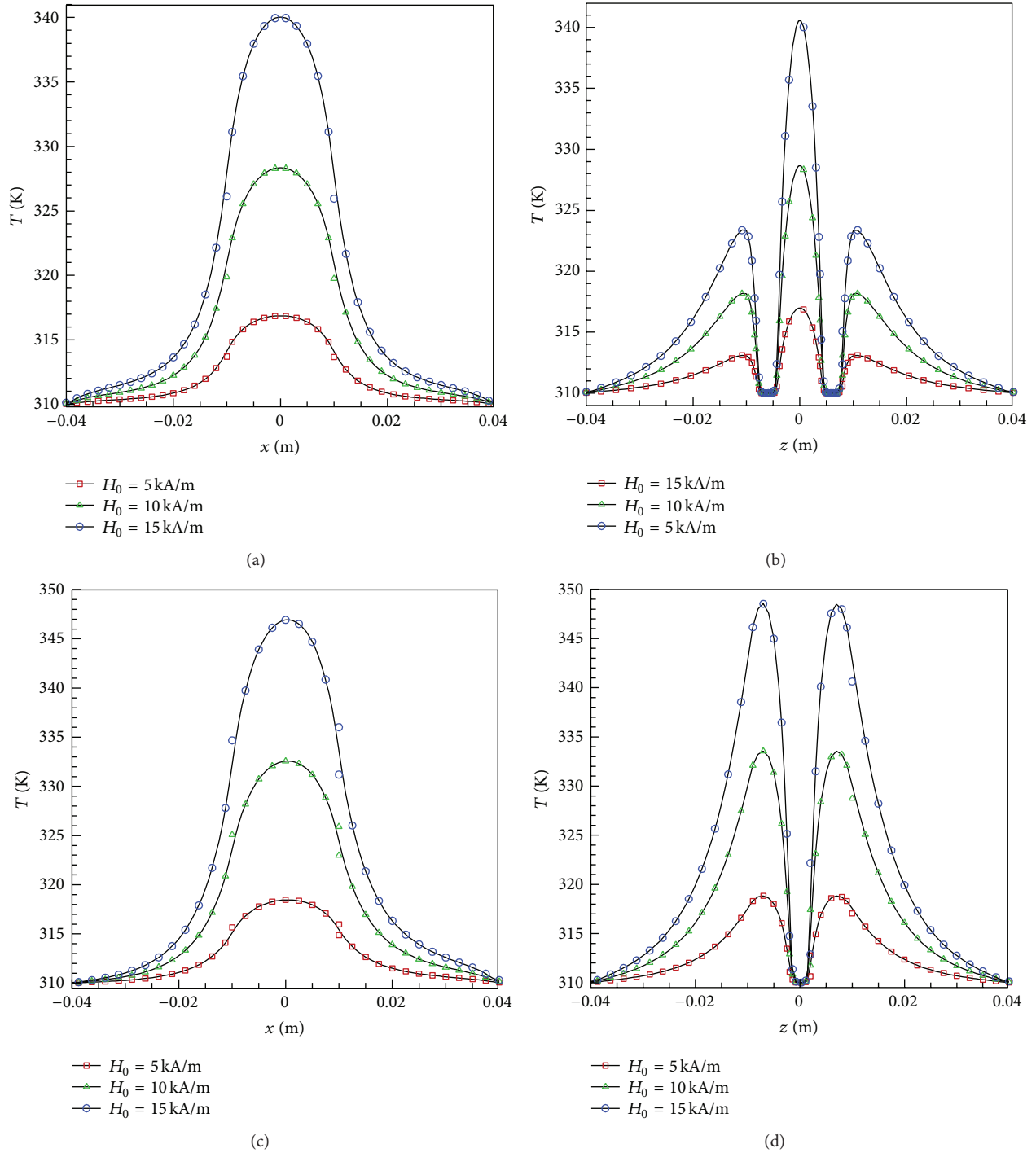


FIGURE 16: Axial variation of temperature profile for different external magnetic field intensity: (a) along x -direction and (b) along z -direction for CVTT model and (c) along x -direction and (d) along z -direction for SATT model.

The axial variation of temperature based on the above-mentioned drug loading criterion is plotted for the CVTT model only along x - and z -direction, respectively (ref. Figures 20(a) and 20(b)). From the figure, it is quite interesting to note that the linear model predicts the highest maximum temperature compared to all the other types of distribution

considered herein. Both the linear model and parabolic model predicts almost same temperature within the healthy tissue, but there is a considerable variation in the temperature prediction within the tumor zone.

Figures 21(a)–21(f) show the temperature profile across different plane for the linear and parabolic drug distribution

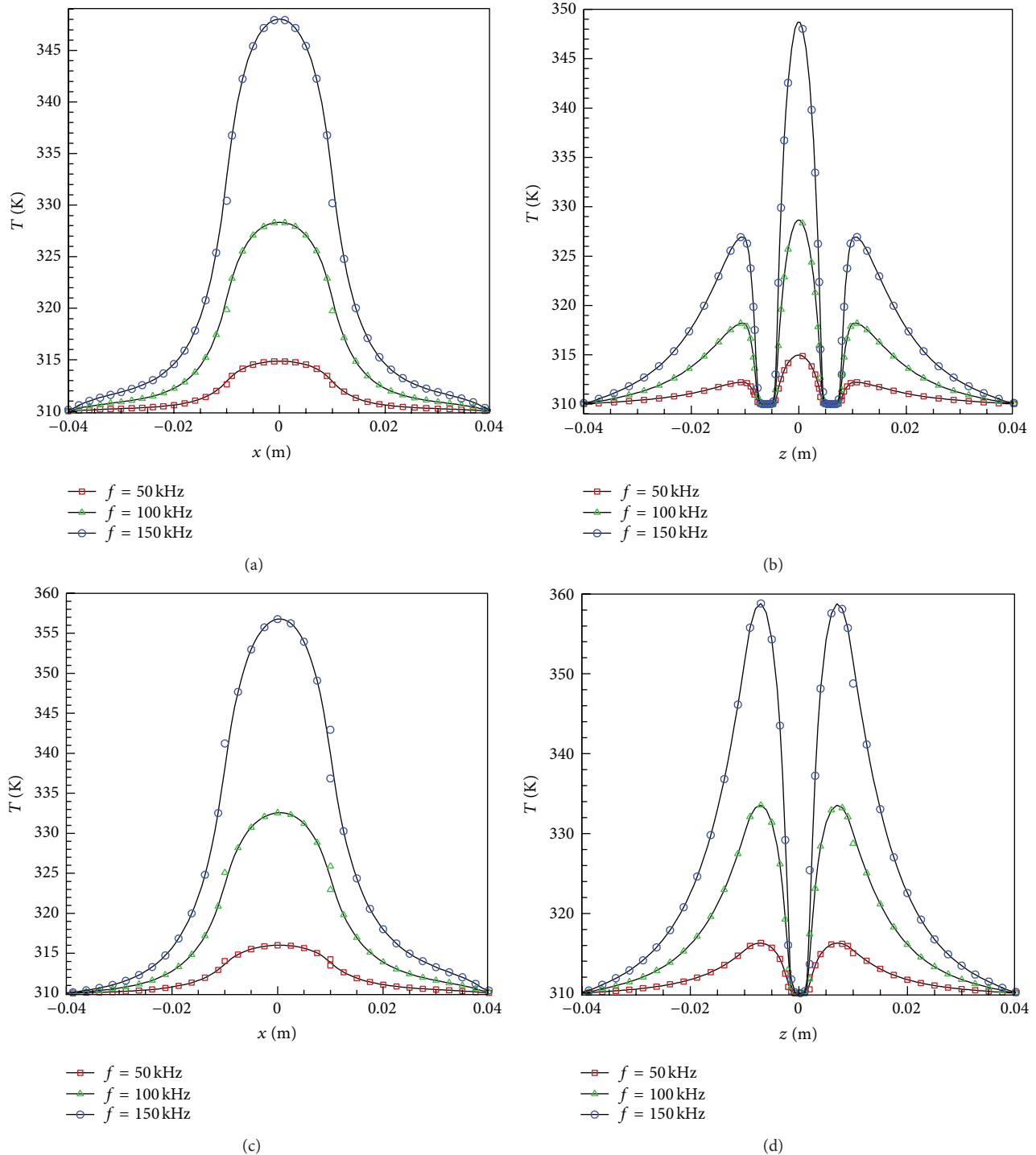


FIGURE 17: Axial variation of temperature profile for different external magnetic frequency: (a) along x -direction and (b) along z -direction for CVTT model and (c) along x -direction and (d) along z -direction for SATT model.

inside the tumor. Comparing the result it is quite clear to note that the linear model predicts overall higher value of temperature in the tumor region.

4. Conclusion

In this paper ANSYS FLUENT is used for solving the three-dimensional form of Pennes Bioheat Transfer Equation to

predict the temperature distribution and thermal effects of MNPs on tissues embedded with large blood vessels during magnetic hyperthermia using different vascular models. To show the effect of MNPs dispersion on temperature distributions, firstly the effect of different parameters such as induction and frequency of the magnetic field and the MNPs volume fraction was studied along with the effect of vascular

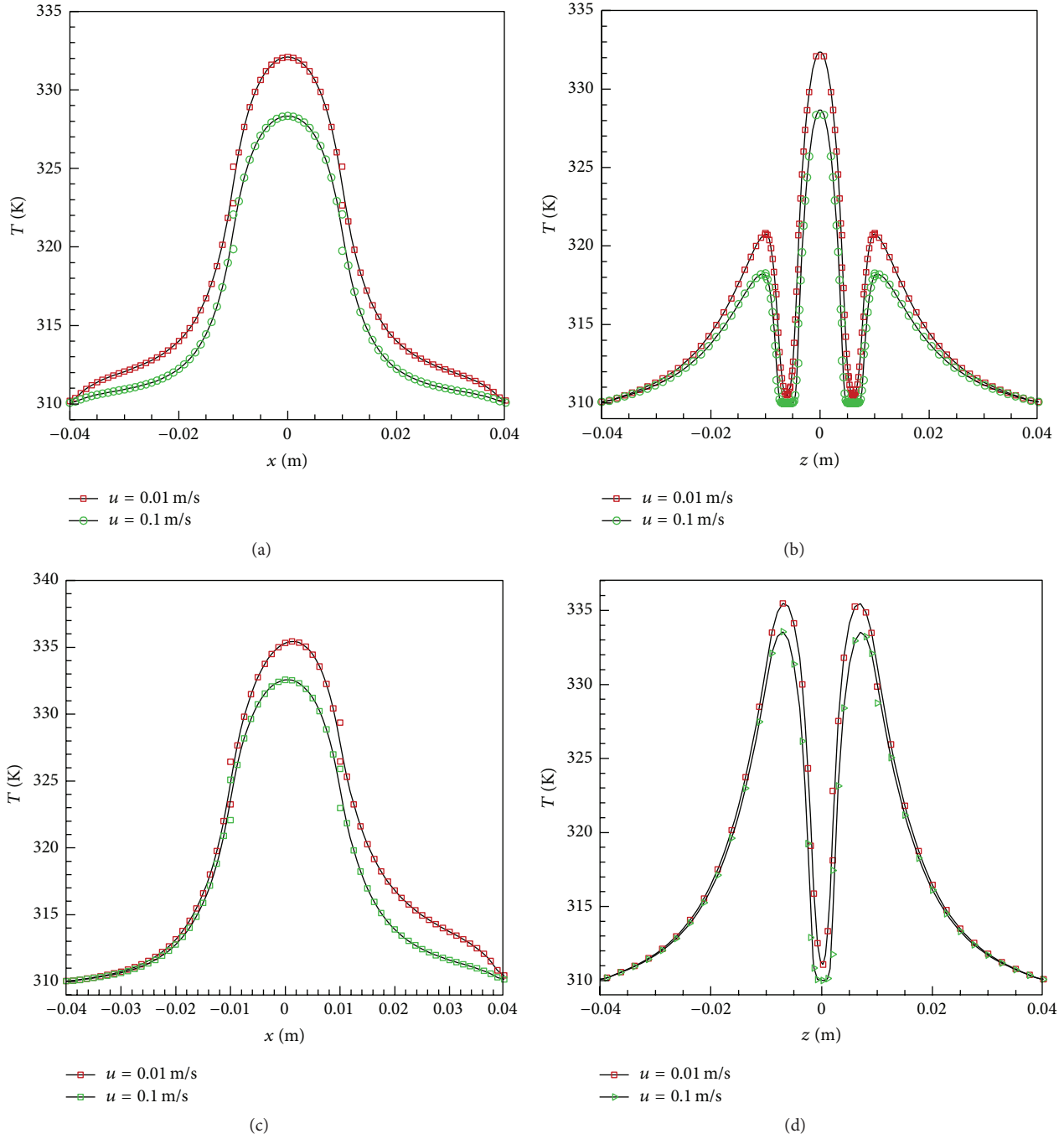


FIGURE 18: Axial variation of temperature profile for different blood velocity due to vascular congestion: (a) along x -direction and (b) along z -direction for CVTT model and (c) along x -direction and (d) along z -direction for SATT model.

congestion. The simulation allows the optimization of the main parameters which influence strongly the heating of the tumor in the therapeutic temperature range and better control of temperature through treatment planning. Based on the simulation results the following are the important conclusions:

(1) For the three different vascular models considered herein, the CVTT model predicts much more cooling

effect compared to other two geometries, which clearly suggest that selection of proper input parameters is quite an important task to achieve a therapeutic temperature throughout the tumor region.

(2) It is observed that the temperature has a minimum value in the place where the blood vessel is located.

(3) Out of the three different magnetic materials considered over here, though fccFePt predicts quite

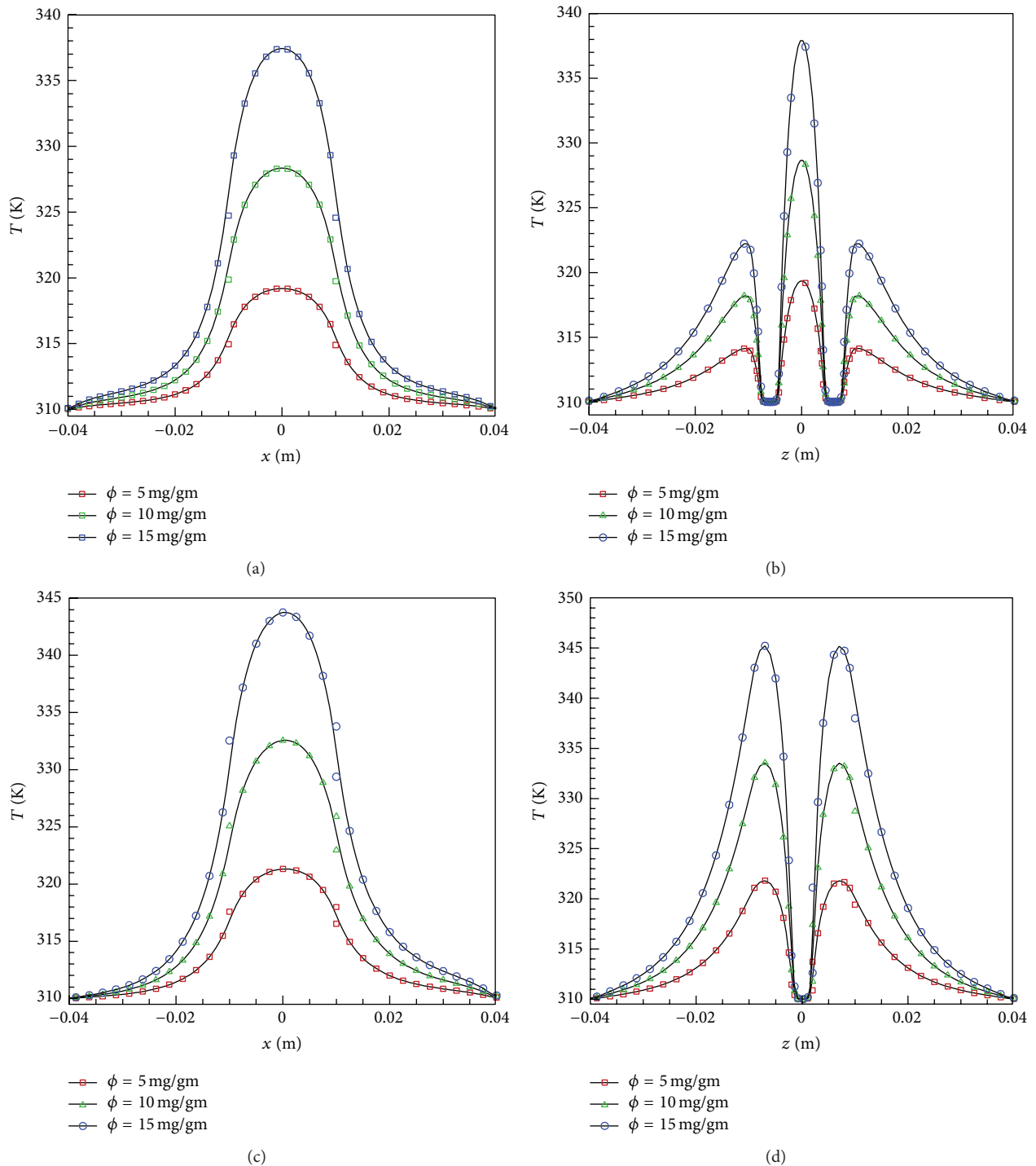


FIGURE 19: Axial variation of temperature profile for different volume fraction: (a) along x -direction and (b) along z -direction for CVTT model and (c) along x -direction and (d) along z -direction for SATT model.

a high value of temperature at the tumor center, from the biocompatibility point of view, Iron oxide magnetite nanoparticles are preferred. For all the clinical application superparamagnetic particles are recommended with an alternating magnetic field with an amplitude range of 5–15 kA/m and frequency in the range of 50–150 kHz. As a result, 19 nm magnetite

MNPs are able to raise the temperature of the tumor above 42.5°C with the dose of 10 mg of magnetite MNP per gram of tumor.

(4) Results show that increase in magnetic field strength, frequency, and volume fraction will increase the temperature within the tumor. The prediction of

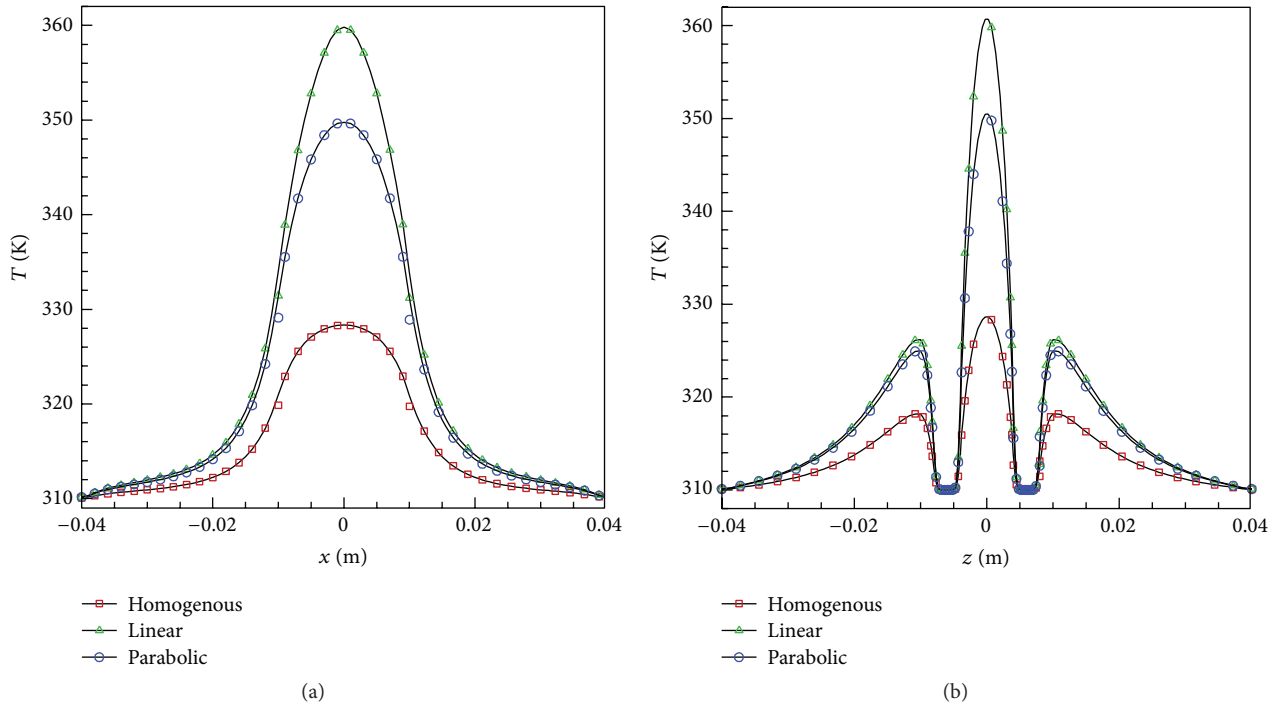


FIGURE 20: Axial variation of temperature profile for different drug distribution pattern inside the tumor for CVTT model: (a) along x -direction and (b) along z -direction.

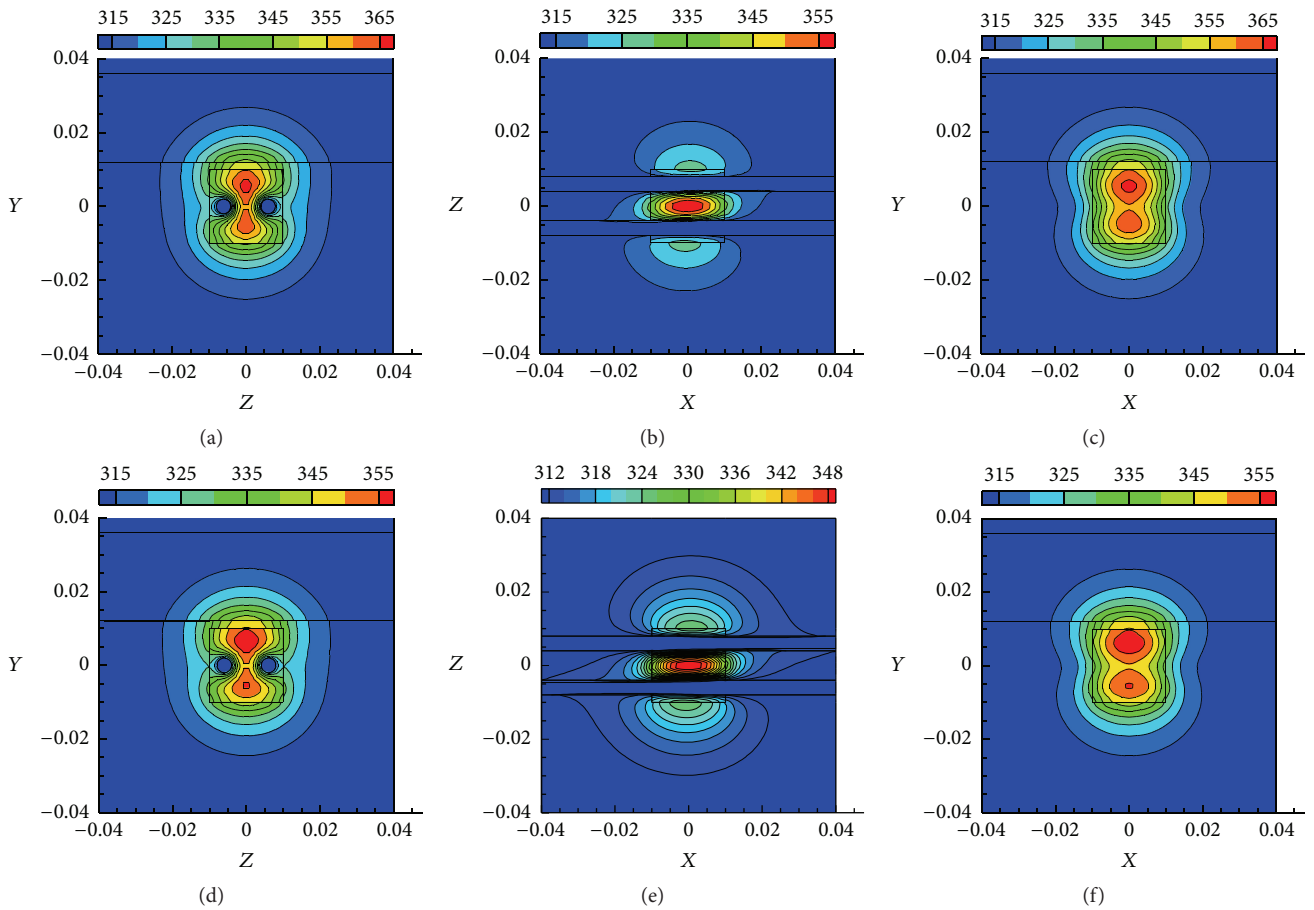


FIGURE 21: Temperature profile for two different MNP distribution patterns along three planes for the CVTT model only: (a, b, and c) linear distribution and (d, e, and f) parabolic distribution.

maximum temperature value is somewhat higher for the SATT model compared to the CATT model.

- (5) The cooling effect of the blood vessel is intensified by the higher blood velocity. On the other hand a smaller value of blood velocity can maintain the therapeutic temperature range within the tumor.
- (6) The MNPs concentration is a major parameter which needs to be optimized properly in order to obtain the therapeutic temperature range within the tumor. A high MNP concentration leads to an increase of temperature within the tumor thereby reducing the cooling effect.
- (7) The results certainly proved that the proper use of MFH can provide accurate temperature control for a tumor with minimal side effects.
- (8) The effect of MNPs dispersion for homogenous, parabolic, and liner distribution was also investigated and the result clearly suggests that the linear distribution predicts quite a high value of temperature within the tumor region, which certainly justifies the tumor necrosis instead of healthy tissue necrosis.

Hence, from the design point of view the selection of these parameters is quite important.

The results provide useful design basis for in vitro setup for the investigation of MFH in the living tissue.

Competing Interests

The authors declare that they have no competing interests.

Acknowledgments

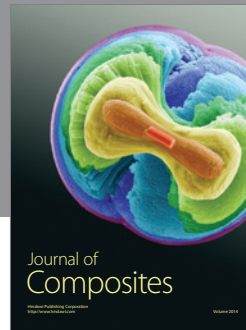
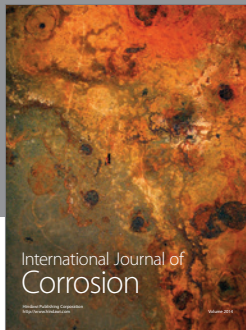
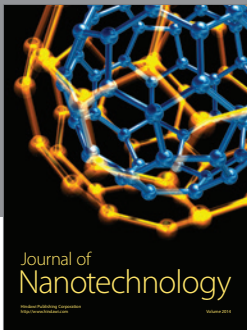
The authors gratefully acknowledge the financial support from the DST under SERC FAST TRACK project (Ref. no. SERC/ET-0173/2011). The authors also like to acknowledge Professor Amitava Datta and Dr. Ranjan Ganguly of Power Engineering Department, Jadavpur University, for their valuable discussions.

References

- [1] Y. He, M. Shirazaki, H. Liu, R. Himeno, and Z. Sun, "A numerical coupling model to analyze the blood flow, temperature, and oxygen transport in human breast tumor under laser irradiation," *Computers in Biology and Medicine*, vol. 36, no. 12, pp. 1336–1350, 2006.
- [2] A. Chichel, J. Skowronek, M. Kubaszewska, and M. Kanikowski, "Hyperthermia—description of a method and a review of clinical applications," *Reports of Practical Oncology and Radiotherapy*, vol. 12, no. 5, pp. 267–275, 2007.
- [3] C. A. Perez and S. A. Sapareto, "Thermal dose expression in clinical hyperthermia and correlation with tumor response/control," *Cancer Research*, vol. 44, supplement 10, pp. 4818s–4825s, 1984.
- [4] J. J. W. Lagendijk, "Hyperthermia treatment planning," *Physics in Medicine and Biology*, vol. 45, pp. R61–R76, 2000.
- [5] P. Moroz, S. K. Jones, and B. N. Gray, "Magnetically mediated hyperthermia: current status and future directions," *International Journal of Hyperthermia*, vol. 18, no. 4, pp. 267–284, 2002.
- [6] S. Maenosono and S. Saita, "Theoretical assessment of FePt nanoparticles as heating elements for magnetic hyperthermia," *IEEE Transactions on Magnetics*, vol. 42, no. 6, pp. 1638–1642, 2006.
- [7] C.-T. Lin and K.-C. Liu, "Estimation for the heating effect of magnetic nanoparticles in perfused tissues," *International Communications in Heat and Mass Transfer*, vol. 36, no. 3, pp. 241–244, 2009.
- [8] J. Overgaard, D. Gonzalez, M. C. C. H. Hulshof et al., "Hyperthermia as an adjuvant to radiation therapy of recurrent or metastatic malignant melanoma. A multicentre randomized trial by the European Society for Hyperthermic Oncology," *International Journal of Hyperthermia*, vol. 25, no. 5, pp. 323–334, 2009.
- [9] A. Jordan, R. Scholz, K. Maier-Hauff et al., "Presentation of a new magnetic field therapy system for the treatment of human solid tumors with magnetic fluid hyperthermia," *Journal of Magnetism and Magnetic Materials*, vol. 225, no. 1-2, pp. 118–126, 2001.
- [10] J. Liu and Z. S. Deng, *Physics of Tumor Hyperthermia*, Science Press, Beijing, China, 2008.
- [11] B. Thiesen and A. Jordan, "Clinical applications of magnetic nanoparticles for hyperthermia," *International Journal of Hyperthermia*, vol. 24, no. 6, pp. 467–474, 2008.
- [12] R. Hergt and S. Dutz, "Magnetic particle hyperthermia—biophysical limitations of a visionary tumour therapy," *Journal of Magnetism and Magnetic Materials*, vol. 311, no. 1, pp. 187–192, 2007.
- [13] M. Pavel and A. Stancu, "Study of the optimum injection sites for a multiple metastases region in cancer therapy by using MFH," *IEEE Transactions on Magnetics*, vol. 45, no. 10, pp. 4825–4828, 2009.
- [14] N. Lupu, H. Chiriac, S. Corodeanu, and G. Ababei, "Development of Fe-Nb-Cr-B glassy alloys with low curie temperature and enhanced soft magnetic properties," *IEEE Transactions on Magnetics*, vol. 47, no. 10, pp. 3791–3794, 2011.
- [15] R. Hergt, W. Andrae, C. G. d'Ambly et al., "Physical limits of hyperthermia using magnetite fine particles," *IEEE Transactions on Magnetics*, vol. 34, no. 5, pp. 3745–3754, 1998.
- [16] T.-L. Horng, W.-L. Lin, C.-T. Liauh, and T.-C. Shih, "Effects of pulsatile blood flow in large vessels on thermal dose distribution during thermal therapy," *Medical Physics*, vol. 34, no. 4, pp. 1312–1320, 2007.
- [17] M. C. Kolios, M. D. Sherar, and J. W. Hunt, "Large blood vessel cooling in heated tissues: a numerical study," *Physics in Medicine and Biology*, vol. 40, no. 4, pp. 477–494, 1995.
- [18] T.-C. Shih, H.-S. Kou, and W.-L. Lin, "The impact of thermally significant blood vessels in perfused tumor tissue on thermal dose distributions during thermal therapies," *International Communications in Heat and Mass Transfer*, vol. 30, no. 7, pp. 975–985, 2003.
- [19] Z.-P. Chen and R. B. Roemer, "The effects of large blood vessels on temperature distributions during simulated hyperthermia," *Journal of Biomechanical Engineering*, vol. 114, no. 4, pp. 473–481, 1992.
- [20] Z. S. Deng and J. Liu, "Monte Carlo simulation of the effects of large blood vessels during hyperthermia," in *Computational and Information Science: First International Symposium, CIS 2004*,

Shanghai, China, December 16–18, 2004. *Proceedings*, vol. 3314 of *Lecture Notes in Computer Science*, pp. 437–442, Springer, Berlin, Germany, 2005.

- [21] H. J. Wang, W. Z. Dai, and A. Bejan, “Optimal temperature distribution in a 3D triple-layered skin structure embedded with artery and vein vasculature and induced by electromagnetic radiation,” *International Journal of Heat and Mass Transfer*, vol. 50, no. 9–10, pp. 1843–1854, 2007.
- [22] V. A. Atsarkin, L. V. Levkin, V. S. Posvyanskiy et al., “Solution to the bioheat equation for hyperthermia with $\text{La}(1-x)\text{Ag}(y)\text{MnO}(3-\delta)$ nanoparticles: the effect of temperature autostabilization,” *International Journal of Hyperthermia*, vol. 25, no. 3, pp. 240–247, 2009.
- [23] J.-H. Lee, J.-T. Jang, J.-S. Choi et al., “Exchange-coupled magnetic nanoparticles for efficient heat induction,” *Nature Nanotechnology*, vol. 6, no. 7, pp. 418–422, 2011.
- [24] L.-Y. Zhang, H.-C. Gu, and X.-M. Wang, “Magnetite ferrofluid with high specific absorption rate for application in hyperthermia,” *Journal of Magnetism and Magnetic Materials*, vol. 311, no. 1, pp. 228–233, 2007.
- [25] P. Di Barba, F. Dughiero, and E. Sieni, “Synthesizing distributions of magnetic nanoparticles for clinical hyperthermia,” *IEEE Transactions on Magnetics*, vol. 48, no. 2, pp. 263–266, 2012.
- [26] P. Di Barba, F. Dughiero, and E. Sieni, “Synthesizing a nanoparticle distribution in magnetic fluid hyperthermia,” *COMPEL*, vol. 30, no. 5, pp. 1507–1516, 2011.
- [27] R. E. Rosensweig, “Heating magnetic fluid with alternating magnetic field,” *Journal of Magnetism and Magnetic Materials*, vol. 252, no. 1–3, pp. 370–374, 2002.
- [28] J. Carrey, B. Mehdaoui, and M. Respaud, “Simple models for dynamic hysteresis loop calculations of magnetic single-domain nanoparticles: application to magnetic hyperthermia optimization,” *Journal of Applied Physics*, vol. 109, no. 8, Article ID 083921, pp. 1–17, 2011.
- [29] W. Andrä, C. G. D. D’Ambly, R. Hergt, I. Hilger, and W. A. Kaiser, “Temperature distribution as function of time around a small spherical heat source of local magnetic hyperthermia,” *Journal of Magnetism and Magnetic Material*, vol. 194, pp. 197–203, 1999.
- [30] ANSYS® Academic CFD Research 14.5, Ansys, Inc.
- [31] A. Miaskowski and B. Sawicki, “Magnetic fluid hyperthermia modeling based on phantom measurements and realistic breast model,” *IEE Transactions on Biomedical Engineering*, vol. 60, no. 7, pp. 1806–1813, 2013.



Hindawi

Submit your manuscripts at
<http://www.hindawi.com>

